Tuning Localized Surface Plasmon Resonance in Scanning Near-Field Optical Microscopy Probes

12 AUTHORS, INCLUDING:

Benjamin Fragneaud
Federal University of Juiz de Fora
16 PUBLICATIONS **291** CITATIONS

SEE PROFILE

Juha Riikonen
Aalto University
57 PUBLICATIONS **335** CITATIONS

SEE PROFILE

Ado Jorio
Federal University of Minas Gerais
281 PUBLICATIONS **18,445** CITATIONS

SEE PROFILE

Luiz Gustavo Cançado
Federal University of Minas Gerais
**62** PUBLICATIONS **3,997** CITATIONS

SEE PROFILE

Tuning Localized Surface Plasmon Resonance in Scanning Near-Field Optical Microscopy Probes

Thiago L. Vasconcelos,*,†,‡ Bráulio S. Archanjo,‡ Benjamin Fragneaud,§ Bruno S. Oliveira,‡ Juha Riikonen,⊥ Changfeng Li,⊥ Douglas S. Ribeiro,† Cassiano Rabelo,† Wagner N. Rodrigues,† Ado Jorio,† Carlos A. Achete,‡,‖ and Luiz Gustavo Cançado*,†,‡

†Departamento de Física, Universidade Federal de Minas Gerais, Belo Horizonte, MG 30123-970, Brazil, ‡Divisão de Metrologia de Materiais, Instituto Nacional de Metrologia, Qualidade e Tecnologia (INMETRO), Duque de Caxias, RJ 25250-020, Brazil, §Departamento de Física, Universidade Federal de Juiz de Fora, Juiz de Fora, MG 36036-900, Brazil, ⊥Department of Micro- and Nanosciences, Aalto University, Tietotie 3, 02150 Espoo, Finland, and ‖Departamento de Engenharia Metalúrgica e de Materiais, Universidade Federal do Rio de Janeiro, Rio de Janeiro, RJ 21941-972, Brazil

ABSTRACT A reproducible route for tuning localized surface plasmon resonance in scattering type near-field optical microscopy probes is presented. The method is based on the production of a focused-ion-beam milled single groove near the apex of electrochemically etched gold tips. Electron energy-loss spectroscopy and scanning transmission electron microscopy are employed to obtain highly spatially and spectroscopically resolved maps of the milled probes, revealing localized surface plasmon resonance at visible and near-infrared wavelengths. By changing the distance L between the groove and the probe apex, the localized surface plasmon resonance energy can be fine-tuned at a desired absorption channel. Tip-enhanced Raman spectroscopy is applied as a test platform, and the results prove the reliability of the method to produce efficient scattering type near-field optical microscopy probes.
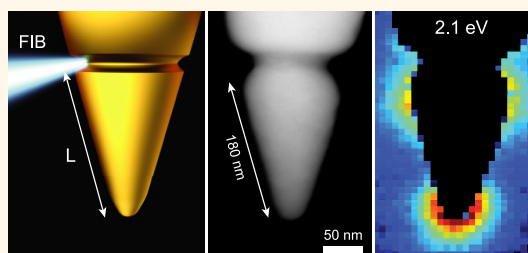
KEYWORDS: localized surface plasmon resonance · near-field · SNOM · EELS · FIB · TERS

Localized surface plasmon is a collective oscillation of conduction electrons occurring on the surface of subwavelength metal nanostructures.[1,2] A remarkable characteristic of the localized surface plasmon resonance (LSPR) phenomena is that the resonance energy can be tuned by changing the size and shape of the host nanostructure,[1,3−7] which has driven great nanoengineering efforts toward the morphological control and characterization of plasmonic nanostructures.[1,2] Among numerous technological applications for LSPR, the scanning near-field optical microscopy (SNOM) has drawn special attention due to its high potential for optical characterization in the nanometer scale.[8−16]

In the apertureless SNOM type, a metal nanostructure is positioned near the sample's surface to act as a nanoantenna that transfers the information contained in the near-field to the far-field, enabling subwavelength spatial resolution solely defined by the size of the nanostructure.[8,9,11−13,15−18]

Different approaches for producing efficient SNOM probes have been reported in the literature, namely, nanoparticles attached to the apex of scanning probe tips,[19−21] Au and Ag pyramids made by template-striped lithography,[22−24] thermal evaporation of thin metal films on standard atomic force microscopy (AFM) tips,[25,26] FIB milled grating coupled Au tips with broad bandwidth for far-field background suppression,[27] and FIB milled bowtie nanoaperture Al probes with broadband field enhancement for single molecule fluorescence studies.[28] However, none of these processes has provided a reproducible control of LSPR energy in the visible range, and the challenge resides on the intrinsical difficulties to perform particle shaping at nanoscale. Recently, Huth et al.[29] developed a resonate-antenna suitable for infrared SNOM. For that, the authors produced gold tips with sizes varying from 500 nm to a few micra, and good control of the LSPR energy was achieved by sizing the tip using a focused ion beam (FIB) setup. The drawback in this
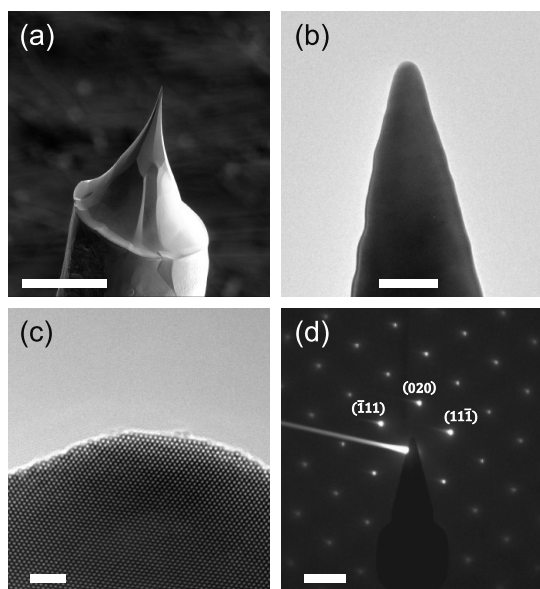
Figure 1. (a) SEM image of a gold tip produced by electrochemical etching. (b) TEM image of the tip, magnified at the apex. (c) Lattice resolved TEM image of the tip apex, exposing the gold crystal structure. (d) Electron diffraction pattern of the same region as shown in panel (c), in the [101]-zone axis. Scale bars: 50 μm, 100 nm, 2 nm, and 4 nm^{-1}, respectively.
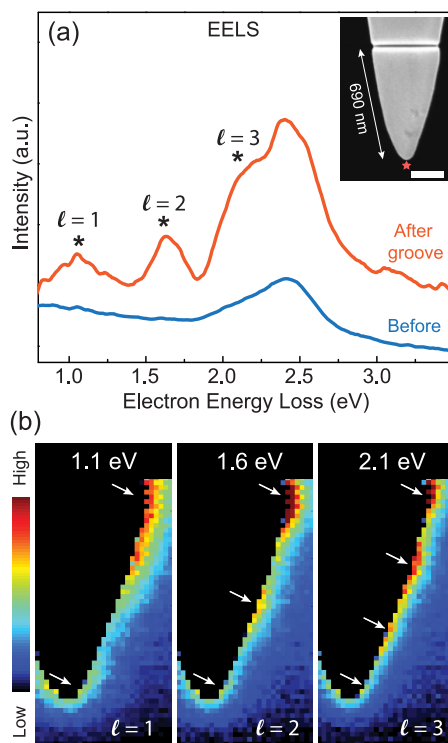

Figure 2. EELS analysis of an electrochemically etched gold tip, with an FIB-milled groove located 690 nm far from the apex. (a) EELS spectra acquired at the vicinity of the tip apex before (blue) and after (red) FIB manipulation. The inset shows an SEM image of the tip after FIB milling, in which the groove can be observed (scale bar: 100 nm). (b) EELS maps at 1.1 eV (left panel), 1.6 eV (middle) and 2.1 eV (right), respectively, obtained after FIB manipulation. The white arrows highlight the LSPR hot spots.

case is the expensive and time-consuming FIB shaping process, since the entire gold structure is FIB-milled to the final narrow cone-like shape.

Here we introduce a reproducible protocol to generate scattering type SNOM probes with well-defined LSPR energy in the visible/near-infrared range. The method consists of drawing a single FIB-milled transversal groove near the apex of an electrochemically etched gold tip. As theoretically proposed,[30−32] the confinement processes due to the presence of the groove generates LSPR at the probe apex, and we use electron energy loss spectroscopy (EELS) combined with scanning transmission electron microscopy (STEM) to investigate the plasmonic properties before and after FIB manipulation. The results reveal that these properties are linked to the distance L between the groove and the apex of the gold probe, and by varying this single parameter we are able to tune the LSPR energy. As a proof of functionality, we perform tip-enhanced Raman scattering (TERS) experiments in graphene using the FIB-milled probes with suitable LSPR energy. The dependence of the Raman response on the tip−sample distance confirms the near-field character of the enhanced signal. Signal enhancement values on the order of 250 were obtained from the tip approach data, and this value is comparable with enhancement factors previously reported in the literature for TERS experiments performed in graphene[33,34] and carbon nanotubes.[17,35]

RESULTS AND DISCUSSION

Figures 1(a) and (b) show, respectively, scanning electron microscopy (SEM) and transmission electron microscopy (TEM) images of a typical gold tip prepared by electrochemical etching (see details in the Methods section). Prior to the etching process, the gold wire was annealed at 850 °C to improve crystallinity. Figures 1(c) and (d) show, respectively, a lattice resolved TEM image of the tip apex, and the corresponding electron diffraction pattern revealing that the produced gold tips are monocrystalline at the apex. This crystallinity is very important, since it minimizes plasmon damping and avoids undesired thermal losses.[36,37] To create LSPR at the apex of the electrochemically etched gold tips, we FIB-milled a single superficial groove perpendicular to the tip shaft (see the details in the Methods section). The LSPR phenomena is based on the electron cloud confinement in subwavelength sized materials, where the resonance is mediated by the matching between the nanostructure dimension and the effective wavelength of the free electron gas oscillation. In the present case, the groove promotes the confinement of plasmon oscillations parallel to the tip shaft, which is the suitable polarization for a strong local field enhancement at the apex.[38]

Figure 2(a) shows EELS spectra acquired at the vicinity of an etched gold tip before (blue line) and after (red line) FIB manipulation. The inset shows an

SEM image of the tip after FIB milling, in which a groove located 690 nm far from the apex can be observed. Before the manipulation, the EELS spectrum shows a strong absorption peak centered at ~2.4 eV. This peak is related to surface plasmon resonance (SPR) driven by interband transitions connecting upper energy states in the 5d valence band with unoccupied states in the half-filled hybride 6sp band.[3,39,40] Unlike LSPR, morphological changes can only shift the SPR energy by a small factor, and for this reason the SPR absorption in gold is usually observed around 2.4−2.6 eV. In contrast to that, the EELS spectrum obtained after FIB manipulation [red line in Figure 2(a)] presents three new absorption peaks (highlighted with asterisk marks) with energies 1.1, 1.6 and 2.1 eV, which are related to LSPR modes. Figure 2(b) shows EELS maps of the FIB manipulated tip, where the color scale renders the intensity of the absorption peaks observed in the EELS spectrum depicted in Figure 2(a). At 1.1 eV (left panel) only two absorption spots are observed, one close to the apex and the other near the groove. In the middle and right panels, (absorption peaks at 1.6 and 2.1 eV, respectively) three and four absorption spots are observed, respectively. Those EELS maps indicate that the three absorption peaks observed in the EELS spectrum of the FIB manipulated tip correspond to the three first LSPR modes, with the first harmonic mode ($l = 1$) occurring at ~1.1 eV, the second ($l = 2$) at ~1.6 eV, and the third ($l = 3$) at ~2.1 eV.

The first LSPR mode ($l = 1$) is of crucial importance, since it is the one that leads to the higher absorption intensity. So far we have generated the first mode in the infrared range (1.1 eV, or λ = 1130 nm) by making the groove 690 nm far from the apex (Figure 2). Aiming for a first mode of LSPR occurring in the visible range, we milled a groove closer to the tip apex ($L \approx 180$ nm). Figure 3 shows the EELS spectra obtained at the vicinity of the tip apex with (red line) and without (blue line) the groove. Before the FIB manipulation, we again observed the SPR peak centered at ~2.4 eV. After FIB manipulation (red line) a new absorption peak with maxima at 2.1 eV is observed. To confirm that this peak is related to the first LSPR mode, we acquired an EELS hyperspectrum line along the tip surface, from the apex to the groove. The spectra are shown in Figure 3(b), and the white dots in the STEM image aside indicate the position where each spectrum was acquired. The SPR peak at ~2.5 eV is present in all spectra. In the other hand, a new peak at ~2.1 eV can be only observed in the spectra acquired near the apex and the groove. The EELS map at 2.1 eV [Figure 3(c)] confirms this result, and unambiguously assign this feature to the first LSPR mode generated by the FIB-milled groove. Figure 3(d) shows the EELS map at 2.5 eV, where the delocalized SPR absorption can be observed all over the tip surface.

To gain insight on the LSPR generation process, we have performed *discrete-dipole approximation* (DDA)
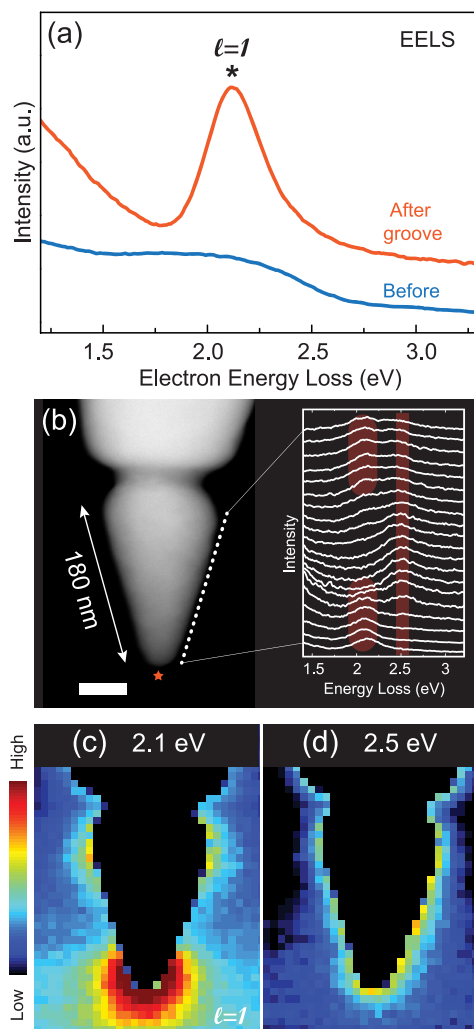

Figure 3. EELS analysis of an electrochemically etched gold tip with a FIB-milled groove located 180 nm far from the apex. (a) EELS spectra acquired at the apex before (blue) and after (red) FIB manipulation. (b) STEM-HAADF image of the tip obtained after FIB manipulation (scale bar: 50 nm). The graphics show a hyperspectral data set (20 spectra) acquired along the tip surface, from the apex to the groove. The white dots in the STEM image indicate the position where each spectrum was acquired. (c,d) EELS intensity maps plotted at 2.1 and 2.5 eV, respectively.

simulation of the EELS response in finite gold cones (see the Methods section for details).[41,42] Figure 4(a) shows simulated EELS spectra of four different gold cones (different lengths L), all of them with the same open angle (32°) and apex diameter (30 nm), as for the tip analyzed in Figure 3. All spectra show the presence of a strong absorption peak (assigned to the dipolar resonance mode) that blue-shifts with the cone shortening (L decreasing). We can also notice the presence of a much less intense peak at 2.5 eV (assigned as the SPR absorption peak), which is just slightly affected by variations on the lateral length L. Figure 4(b) shows the simulated EELS intensity map at 2.15 eV for the cone with L = 195 nm. The simulated map is in excellent agreement with the experimental map show in
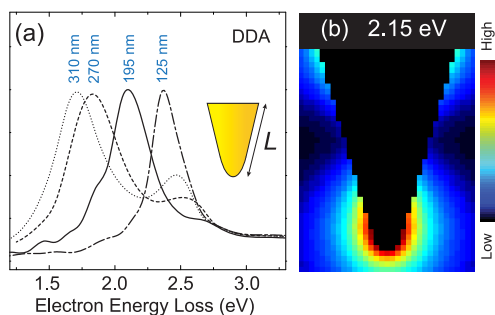
Figure 4. (a) DDA simulated EELS spectra analyzed at the apex of four different gold cones (L = 125, 195, 270, and 310 nm, as indicated on the top of each corresponding spectrum). (b) DDA simulation of the EELS intensity map for a gold cone with L = 195 nm, plotted at 2.15 eV.

Figure 3(c), revealing two hot spots, one at the tip apex and the other (less intense) at the groove.

The next step in our analysis is to establish a relation between the length L and the wavelength λ of the incident (or scattered) radiation field to promote LSPR in the FIB-milled s-SNOM probes. According to the classical dipole antenna theory applied to a thin rod, this connection is simply $L = \lambda/2$.[43] However, this relation is based on the premise that the antenna is made of a perfect metal with infinity conductivity, into which the radiation field does not penetrate. Although this approach is still valid for antennas that resonate in the long-wavelength range (microwave regime), a most realistic relation (suitable for optical frequencies) has been recently introduced by Novotny,[9] who proposed that the plasmon oscillation generated by the interaction between the radiation field and the free electron gas inside the metal nanostructure holds an effective wavelength λ_{eff} (shorter than λ) with the form

$$\lambda_{eff} = n_1 + n_2 \left(\frac{\lambda}{\lambda_p} \right) \qquad (1)$$

where n_1 and n_2 are parameters that depend on the geometry and material properties of the antenna, and λ_p is the plasmon frequency (for gold, $\lambda_p = 138$ nm).

Figure 5(a) shows the plot of the lateral length L of four different FIB-milled gold tips as a function of the first LSPR mode wavelength $\lambda_{LSPR}^{(1)}$ (filled symbols) extracted from experimental EELS data [corresponding spectra shown in Figure 5(b)]. The upper horizontal axis is scaled with the corresponding first LSPR mode energy $E_{LSPR}^{(1)}$ for reference.[56] We also included the theoretical results (empty symbols) obtained from DDA simulation [spectra shown in Figure 4(a)]. Notice that the theoretical results follows the same trend as the experimental data, for which the farther from the apex the groove is (L increases), the longer $\lambda_{LSPR}^{(1)}$ takes ($E_{LSPR}^{(1)}$ decreases). The plot in Figure 5(a) clearly shows a linear relation between L and $\lambda_{LSPR}^{(1)}$, confirming that the FIB-milled tips behave as optical antennas. The solid line is the fit to the experimental data according to
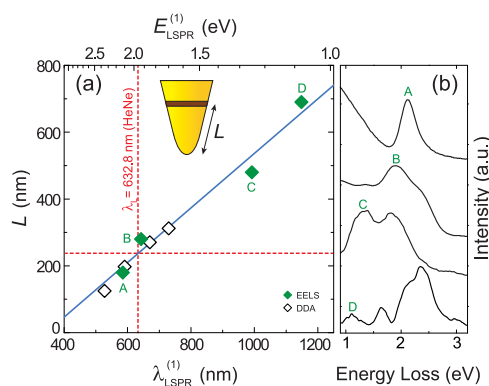

Figure 5. (a) Plot of the of the distance L between the groove and the apex of FIB-milled gold tips as a function of the first LSPR mode wavelength ($\lambda_{LSPR}^{(1)}$). The upper axis is scaled with the corresponding first LSPR mode energy ($E_{LSPR}^{(1)}$). The filled symbols are experimental data extracted from EELS spectra [shown in (b)] obtained from FIB-milled gold tips. The empty symbols are theoretical results from DDA simulation. The solid line is the fit to the experimental data according to eq 1, where we have considered the constraint $L = \lambda_{eff}/2$, together with the resonance condition $\lambda = \lambda_{LSPR}^{(1)}$. Substitution of the output parameters ($n_1 = -560$ nm, $n_2 = 225$ nm) in eq 1 yields $L = -280 + 0.815\lambda$ (eq 2). The vertical dashed line indicate the He–Ne laser wavelength (632.8 nm), and the horizontal dashed line indicate the length L that generates the corresponding LSPR. (b) Experimental EELS spectra. The green letters connect each observed absorption peak to the corresponding data point in (a).

eq 1, where we have considered the constraint $L = \lambda_{eff}/2$, and the resonance condition $\lambda = \lambda_{LSPR}^{(1)}$. With the fitting output parameters ($n_1 = -560$ nm, $n_2 = 225$ nm), we can set up the relation

$$L = -280 + 0.815\lambda \qquad (2)$$

(L and λ in nm units), which can be used as a guide for tuning LSPR in gold FIB-milled SNOM probes.

We have performed tip-enhanced Raman scattering (TERS) experiments to test the liability of the FIB-milled gold tips. The experimental setup is similar to that described in ref.[17] The experiment was carried out using a HeNe laser source (excitation wavelength $\lambda_L = 632.8$ nm), and the results are summarized in Figure 6. Guided by eq 2, we produced a FIB-milled gold tip with $L \approx 240$ nm [SEM image shown in Figure 6(a)], which is expected to promote an LPSR match with the excitation laser source [see dashed lines in Figure 5(a)]. Figure 6(b,c) show correspondent confocal and near-field hyperspectral images (obtained with and without the FIB-milled gold tip, respectively) of a CVD-grown twisted bilayer graphene (tBLG).[44] The color scale in both images renders the amplitude of the bond stretching G mode (~1580 cm^{-1}). The comparison between both images highlights the considerably higher spatial resolution achieved in the near-field image [Figure 6(c)]. The profits in signal enhancement and spatial resolution promoted by the presence of the tip can be clearly noticed in the upper panel of Figure 6(d), which shows
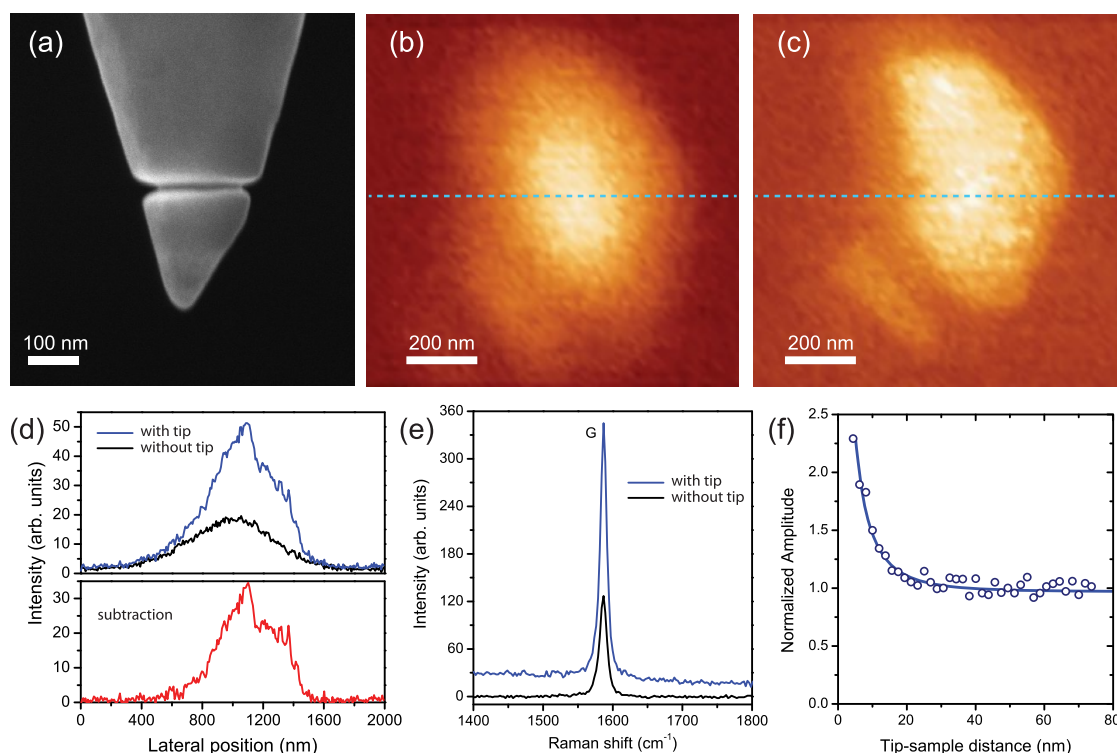
Figure 6. Tip-enhanced Raman scattering (TERS) data carried out using a HeNe laser source (excitation wavelength λ_L = 632.8 nm). (a) SEM image of the FIB-milled gold tip used in the experiment. To promote the match between λ_L and the first LSPR mode wavelength ($\lambda_{LSPR}^{(1)}$), the groove was milled at $L \approx 240$ nm, following the protocol established in eq 2. (b,c) Correspondent confocal and near-field hyperspectral images of a twisted bilayer graphene (tBLG) piece obtained without and with the tip, respectively. The color scale in both images renders the amplitude of the bond stretching G mode ($\sim$1580 cm^{-1}). (d) Upper panel: G mode intensity profiles obtained from hyperspectral scan lines taken along the dashed lines in panels (b,c). Bottom panel: pure near-field intensity profile obtained by the subtraction of the profile taken without the tip (far-field contribution) from the profile taken with the tip. The sharp edges in this intensity profile indicate a spatial resolution of $\sim$40 nm. (e) G band spectra obtained with (blue spectrum) and without (black spectrum) the tip. (f) G mode intensity as a function of the tip–sample distance (approach curve). The empty symbols are experimental data, and the whole data set was normalized by the average intensity obtained when the tip is far from the sample (above 60 nm). The solid line is a fit to the experimental data following the theory proposed in the literature.[33,46]

intensity profiles obtained from hyperspectral scan lines taken along the dashed lines in Figure 6(b,c). The pure near-field contribution is presented in the bottom panel of Figure 6(d), which shows the result of the subtraction of the intensity profile obtained without the tip (far-field contribution) from the profile obtained with the tip. The relatively sharp edges indicate a spatial resolution of $\sim$40 nm, in good agreement with the tip's morphology observed in the SEM image [Figure 6(a)].

Figure 6(e) shows the G band spectra obtained with (blue spectrum) and without (black spectrum) the tip. As shown in the graphics, the Raman response more than doubles when the tip is located near the sample. Taking into consideration that we are probing a two-dimensional system, the observed gain in signal strength corresponds to an expressive enhancement factor. Figure 6(f) shows the plot of the G mode intensity as a function of the tip–sample distance (approach curve). The empty symbols are experimental data, and the whole data set was normalized by the average intensity obtained when the tip is positioned far from the sample (above 60 nm). The highest intensity is obtained when the tip is closest to the

surface ($\sim$5 nm), and this value is $\sim$2.3× larger than that obtained when the tip is far from the surface, revealing that the FIB-milled tip promotes an intensity enhancement of $M \approx 245$.[57] This is an excellent achievement if compared to representative values reported in the literature for TERS experiments performed in graphene[33,34] and carbon nanotubes.[17,35] The solid line in Figure 6(f) is the fit to the experimental data following the theory proposed in ref.,[46] and undoubtedly confirm that the enhancement observed in this experiment is mediated by the near-field contribution to the scattered signal. In order to test for the reproducibility of our method, four additional tips were also tested, and similar results were obtained.

To check for the actual improvement promoted by the presence of the groove, we have measured the field enhancement generated by the Au tips before and after undergo the milling processes. A representative result is presented in Figure 7, showing G band spectra obtained before [Figure 7(a)] and after [Figure 7(b)] the milling process take place. The tip was milled at $L = 240$ nm, which is the same value as for the tip used in the experiment shown in Figure 6
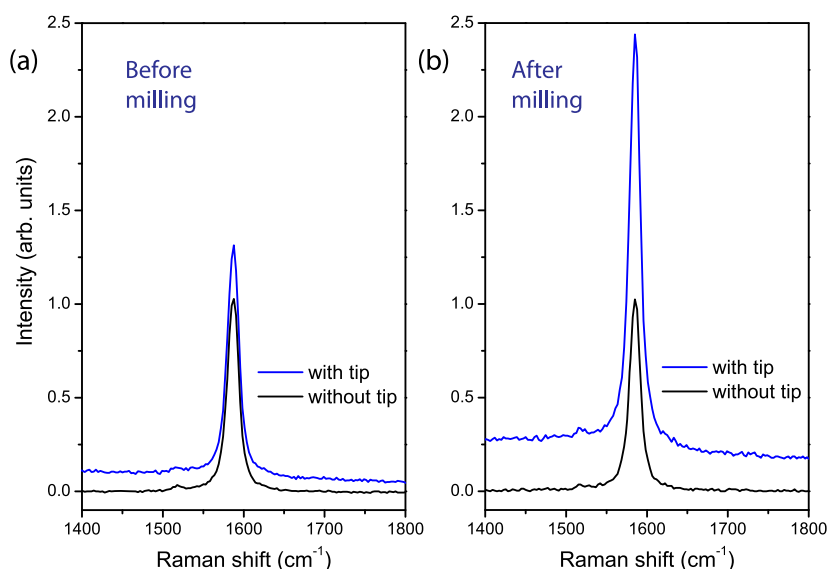
Figure 7. Graphene G band spectra obtained before (a) and after (b) the milling process take place. The tip was milled at $L = 240$ nm, which is the same value as for the tip used in the experiment shown in Figure 6 (proper for $\lambda_L = 632.8$ nm). The blue spectra were obtained in the presence of the tip, and the black spectra were obtained without the tip.

(proper for $\lambda_L = 632.8$ nm). Before the milling process [Figure 7(a)], the G band intensity recorded in the presence of the tip was 1.2× larger than the intensity recorded without the tip, which corresponds to a signal enhancement of $M \approx 38$. After the milling process [Figure 7(b)], the G band intensity recorded in the presence of the tip was found to be 2.1× larger than the intensity recorded without the tip, revealing a signal enhancement of $M \approx 210$. Therefore, we conclude that the milling process can improve the signal enhancement by at least a factor 5.5 ($\approx 210/38$). This is an important test, since the milling process produces Ga^+ implantation into the Au lattice, which could harm the plasmonic properties of the tip. However, the data presented in Figure 7 show that the gain engendered by the presence of the groove overtakes any damage generated by the milling process.

CONCLUSION

We presented a reproducible route to generate SNOM probes with tunable LSPR in the visible/near-infrared range. For that, we have performed FIB milling of a single groove near the apex of electrochemically etched gold tips. Experimental EELS analysis combined with theoretical DDA simulations revealed that the distance L between the groove and the tip apex can be taken as the only parameter to tune the LSPR energy, providing high absorption and scattering efficiencies at desired wavelengths. On the basis of the experimental EELS data, and taking into account the effective wavelength of the plasmon oscillation, we obtained a simple relation eq 2 to guide the LSPR tuning in FIB-milled SNOM probes. The protocol was applied to the production of test SNOM probes applied to TERS experiments. By successfully performing near-field Raman spectroscopy of a twisted-bilayer graphene piece, the FIB-milled tips were proved to work as efficient resonant nanoantennas. The single-step nanofabrication process proposed here opens a new route for increasing the yield of SNOM probes applied to experiments performed in optical frequencies, which has been a strong drawback in the use of near-field spectroscopy as a versatile tool for materials science.

METHODS

Electrochemical Etching of Gold Tips. The conical shaped gold tips were produced by the lamella-dropoff electrochemical etching method.[47] For that we used 100 μm thick gold wire with 99.995% purity, and a 37% HCl solution. For good reproducibility, an automate control of the cathode current is required to interrupt the etching process at the moment the tip is formed. This procedure is needed to avoid extra etching that can result in larger apex diameters.[48] After the etching process is complete, scanning electron microscopy (SEM) was used to select tips with apex diameters smaller than 50 nm, and open angles greater than 20°.

EELS. The EELS technique has recently emerged as one of the most useful tools for the study of LSPR in metal nanostructures,[49,50] and was employed here to analyze the FIB-milled tips. The measurements were performed in a probe-corrected Titan 80/300 setup (FEI Company), operating at 300 kV (accelerating voltage). The system is equipped with gun monochromator and spectrometer, model GIF Tridiem 866, Gatan. The interaction between the incident electron beam and the metal surface was probed with energy resolution beyond 200 meV, allowing for the determination of single-mode LSPR energies in the visible/near-IR range.[51,52] The measurements were performed in scanning transmission electron

microscopy (STEM) mode, providing detailed plasmon absorption maps with subnanometer spatial resolution. To treat the data, a zero-loss peak (ZLP) deconvolution was performed by using a reference spectrum acquired outside the sample.[51,52]

FIB Manipulation. The FIB milling processes were performed using a dual beam microscope equipped with a gallium column, model Helios Nanolab 650 (FEI Company). The accelerating voltage and ion current were set to 30 kV and 7 pA, respectively, generating milled grooves with ~20 nm of width and depth. To avoid surface damage, a single ion image with 300 ns dwell time is performed prior to the milling process. The position of the FIB milled groove is controlled by the dual beam microscope, and variations on the order of ±10 nm can occur.

DDA Simulations. Discrete-dipole approximation (DDA) simulations of EELS spectra were performed using the DDEELS code v2.1.[53] The dipole separation was set as a fixed parameter of 5 nm. The simulations were performed for four different conical tips (different lengths of 125, 195, 270, and 310 nm), all of them having the same apex diameter (30 nm) and open angle (32°). The dielectric constants for gold were taken from ref.[54] Although the DDA simulation is very helpful for understanding the plasmon absorption source, polarization direction, hot spot positions, and the relationship between the energy shift and the morphologic modification, it is important mentioning that, for long structures ($L > 70$ nm), the absolute energy values for the absorption peaks are suspicious. When compared to the experimental data, an energy shift up to 0.7 eV for large structures has been previously reported in the literature.[42,50,55] This shift can be linked to a combination of factors, including roundness of the edge structure,[42] retardation effects,[50] parametrization of the dielectric function[50] and contamination/damaging generated by the e-beam.[55] Our simulations also presented a blue-shift of 0.45 eV, which has been subtracted from the data shown in Figures 4 and 5(a).

Conflict of Interest: The authors declare no competing financial interest.

REFERENCES AND NOTES

1. Kelly, K. L.; Coronado, E.; Zhao, L. L.; Schatz, G. C. The Optical Properties of Metal Nanoparticles: the Influence of Size, Shape, and Dielectric Environment. *J. Phys. Chem. B* **2003**, *107*, 668–677.
2. Petryayeva, E.; Krull, U. J. Localized Surface Plasmon Resonance: Nanostructures, Bioassays and Biosensing—a Review. *Anal. Chim. Acta* **2011**, *706*, 8–24.
3. Scaffardi, L. B.; Tocho, J. O. Size Dependence of Refractive Index of Gold Nanoparticles. *Nanotechnology* **2006**, *17*, 1309–1315.
4. Zoric, I.; Zach, M.; Kasemo, B.; Langhammer, C. Gold, Platinum, and Aluminum Nanodisk Plasmons: Material Independence, Subradiance, and Damping Mechanisms. *ACS Nano* **2011**, *5*, 2535–2546.
5. Anderson, L. J. E.; Payne, C. M.; Zhen, Y.-R.; Nordlander, P.; Hafner, J. H. A Tunable Plasmon Resonance in Gold Nanobelts. *Nano Lett.* **2011**, *11*, 5034–5037.
6. Knight, M. W.; Liu, L.; Wang, Y.; Brown, L.; Mukherjee, S.; King, N. S.; Everitt, H. O.; Nordlander, P.; Halas, N. J. Aluminum Plasmonic Nanoantennas. *Nano Lett.* **2012**, *12*, 6000–6004.
7. Schimpf, A. M.; Thakkar, N.; Gunthardt, C. E.; Masiello, D. J.; Gamelin, D. R. Charge-Tunable Quantum Plasmons in Colloidal Semiconductor Nanocrystals. *ACS Nano* **2013**, *8*, 1065–1072.
8. Martin, Y. C.; Hamann, H. F.; Wickramasinghe, H. K. Strength of the Electric Field in Apertureless Near-Field Optical Microscopy. *J. Appl. Phys.* **2001**, *89*, 5774–5778.
9. Novotny, L. Effective Wavelength Scaling for Optical Antennas. *Phys. Rev. Lett.* **2007**, *98*, 266802–266805.
10. Stöckle, R. M.; Suh, Y. D.; Deckert, V.; Zenobi, R. Nanoscale Chemical Analysis by Tip-Enhanced Raman Spectroscopy. *Chem. Phys. Lett.* **2000**, *318*, 131–136.
11. Hartschuh, A. Tip-Enhanced Near-Field Optical Microscopy. *Angew. Chem.* **2008**, *47*, 8178–8191.
12. Bailo, E.; Deckert, V. Tip-Enhanced Raman Spectroscopy of Single RNA Strands: Towards a Novel Direct-Sequencing Method. *Angew. Chem.* **2008**, *47*, 1658–1661.
13. Yeo, B.-S.; Stadler, J.; Schmid, T.; Zenobi, R.; Zhang, W. Tip-Enhanced Raman Spectroscopy—Its Status, Challenges and Future Directions. *Chem. Phys. Lett.* **2009**, *472*, 1–13.
14. Ogawa, Y.; Yuasa, Y.; Minami, F.; Oda, S. Tip-Enhanced Raman Mapping of a Single Ge Nanowire. *Appl. Phys. Lett.* **2011**, *99*, 053112–053114.
15. Novotny, L.; Hecht, B. *Principles of Nano-Optics*; Cambridge University Press: Cambridge, U.K., 2012.
16. Maciel, I. O.; Anderson, N.; Pimenta, M. A.; Hartschuh, A.; Qian, H.; Terrones, M.; Terrones, H.; Campos-Delgado, J.; Rao, A. M.; Novotny, L.; Jorio, A. Electron and Phonon Renormalization Near Charged Defects in Carbon Nanotubes. *Nat. Mater.* **2008**, *7* (11), 878–883.
17. Cançado, L. G.; Hartschuh, A.; Novotny, L. Tip-Enhanced Raman Spectroscopy of Carbon Nanotubes. *J. Raman Spectrosc.* **2009**, *40*, 1420–1426.
18. Verma, P.; Ichimura, T.; Yano, T.-a.; Saito, Y.; Kawata, S. Nano-Imaging Through Tip-Enhanced Raman Spectroscopy: Stepping Beyond the Classical Limits. *Laser Photonics Rev.* **2010**, *4*, 548–561.
19. Becker, M.; Sivakov, V.; Gösele, U.; Stelzner, T.; Andrä, G.; Reich, H. J.; Hoffmann, S.; Michler, J.; Christiansen, S. H. Nanowires Enabling Signal-Enhanced Nanoscale Raman Spectroscopy. *Small* **2008**, *4*, 398–404.
20. Höppener, C.; Novotny, L. Antenna-Based Optical Imaging Of Single Ca^{2+} Transmembrane Proteins in Liquids. *Nano Lett.* **2008**, *8*, 642–646.
21. Umakoshi, T.; Yano, T.-a.; Saito, Y.; Verma, P. Fabrication of Near-Field Plasmonic Tip by Photoreduction for Strong Enhancement in Tip-Enhanced Raman Spectroscopy. *Appl. Phys. Express* **2012**, *5*, 052001–052003.
22. Lindquist, N. C.; Nagpal, P.; Lesuffleur, A.; Norris, D. J.; Oh, S.-H. Three-Dimensional Plasmonic Nanofocusing. *Nano Lett.* **2010**, *10*, 1369–1373.
23. Johnson, T. W.; Lapin, Z. J.; Beams, R.; Lindquist, N. C.; Rodrigo, S. G.; Novotny, L.; Oh, S.-H. Highly Reproducible Near-Field Optical Imaging with sub-20-nm Resolution Based on Template-Stripped Gold Pyramids. *ACS Nano* **2012**, *6*, 9168–9174.
24. Lindquist, N. C.; Johnson, T. W.; Nagpal, P.; Norris, D. J.; Oh, S.-H. Plasmonic Nanofocusing with a Metallic Pyramid and an Integrated C-Shaped Aperture. *Sci. Rep.* **2013**, *3*, 1857.
25. Yeo, B.-S.; Schmid, T.; Zhang, W.; Zenobi, R. Towards Rapid Nanoscale Chemical Analysis Using Tip-Enhanced Raman Spectroscopy with Ag-Coated Dielectric Tips. *Anal. Bioanal. Chem.* **2007**, *387*, 2655–2662.
26. Weber-Bargioni, A.; Schwartzberg, A.; Cornaglia, M.; Ismach, A.; Urban, J. J.; Pang, Y.; Gordon, R.; Bokor, J.; Salmeron, M. B.; Ogletree, D. F.; *et al.* Hyperspectral Nanoscale Imaging on Dielectric Substrates with Coaxial Optical Antenna Scan Probes. *Nano Lett.* **2011**, *11*, 1201–1207.
27. Berweger, S.; Atkin, J. M.; Olmon, R. L.; Raschke, M. B. Light on the Tip of a Needle: Plasmonic Nanofocusing for Spectroscopy on the Nanoscale. *J. Phys. Chem. Lett.* **2012**, *3*, 945–952.
28. Mivelle, M.; van Zanten, T. S.; Neumann, L.; van Hulst, N. F.; Garcia-Parajo, M. F. Ultrabright Bowtie Nanoaperture

Antenna Probes Studied by Single Molecule Fluorescence. *Nano Lett.* **2012**, *12*, 5972–5978. PMID: 23098104

29. Huth, F.; Chuvilin, A.; Schnell, M.; Amenabar, I.; Krutokhvostov, R.; Lopatin, S.; Hillenbrand, R. Resonant Antenna Probes for Tip-Enhanced Infrared Near-Field Microscopy. *Nano Lett.* **2013**, *13*, 1065–1072.

30. Krug, J. T., II; Sanchez, E. J.; Xie, X. S. Design of Near-Field Optical Probes with Optimal Field Enhancement by Finite Difference Time Domain Electromagnetic Simulation. *J. Chem. Phys.* **2002**, *116*, 10895–10901.

31. Zhang, W.; Cui, X.; Martin, O. J. Local Field Enhancement of an Infinite Conical Metal Tip Illuminated by a Focused Beam. *J. Raman Spectrosc.* **2009**, *40*, 1338–1342.

32. Antosiewicz, T. J.; Wróbel, P.; Szoplik, T. Performance of Scanning Near-Field Optical Microscope Probes with Single Groove and Various Metal Coatings. *Plasmonics* **2011**, *6*, 11–18.

33. Beams, R.; Cançado, L. G.; Oh, S.-H.; Jorio, A.; Novotny, L. Spatial Coherence in Near-Field Raman Scattering. *Phys. Rev. Lett.* **2014**, *113*, 186101–186105.

34. Su, W.; Roy, D. Visualizing Graphene Edges Using Tip-Enhanced Raman Spectroscopy. *J. Vac. Sci. Technol., B* **2013**, *31*, 041808–041813.

35. Cançado, L.; Jorio, A.; Ismach, A.; Joselevich, E.; Hartschuh, A.; Novotny, L. Mechanism of Near-Field Raman Enhancement in One-Dimensional Systems. *Phys. Rev. Lett.* **2009**, *103*, 186101–186104.

36. Roy, D.; Williams, C.; Mingard, K. Single-Crystal Gold Tip for Tip-Enhanced Raman Spectroscopy. *J. Vac. Sci. Technol., B* **2010**, *28*, 631–634.

37. Kusar, P.; Gruber, C.; Hohenau, A.; Krenn, J. R. Measurement and Reduction of Damping in Plasmonic Nanowires. *Nano Lett.* **2012**, *12*, 661–665.

38. Novotny, L.; Bian, R. X.; Xie, X. S. Theory of Nanometric Optical Tweezers. *Phys. Rev. Lett.* **1997**, *79*, 645–648.

39. Politano, A.; Formoso, V.; Chiarello, G. Dispersion and Damping of Gold Surface Plasmon. *Plasmonics* **2008**, *3*, 165–170.

40. Pulisciano, A.; Park, S.; Palmer, R. Surface Plasmon Excitation of Au and Ag in Scanning Probe Energy Loss Spectroscopy. *Appl. Phys. Lett.* **2008**, *93*, 213109–213111.

41. Geuquet, N.; Henrard, L. EELS and Optical Response of a Noble Metal Nanoparticle in the Frame of a Discrete Dipole Approximation. *Ultramicroscopy* **2010**, *110*, 1075–1080.

42. Bigelow, N. W.; Vaschillo, A.; Iberi, V.; Camden, J. P.; Masiello, D. J. Characterization of the Electron- and Photon-Driven Plasmonic Excitations of Metal Nanorods. *ACS Nano* **2012**, *6*, 7497–7504.

43. Milligan, T. A. *Modern Antenna Design*; John Wiley & Sons: New York, 2005.

44. Riikonen, J.; Kim, W.; Li, C.; Svensk, O.; Arpiainen, S.; Kainlauri, M.; Lipsanen, H. Photo-Thermal Chemical Vapor Deposition of Graphene On Copper. *Carbon* **2013**, *62*, 43–50.

45. Stadler, J.; Schmid, T.; Zenobi, R. Developments in and Practical Guidelines for Tip-Enhanced Raman Spectroscopy. *Nanoscale* **2012**, *4*, 1856–1870.

46. Cançado, L. G.; Beams, R.; Jorio, A.; Novotny, L. Theory of Spatial Coherence in Near-Field Raman Scattering. *Phys. Rev. X* **2014**, *4*, 031054–031067.

47. Klein, M.; Schwitzgebel, G. An Improved Lamellae Drop-Off Technique for Sharp Tip Preparation in Scanning Tunneling Microscopy. *Rev. Sci. Instrum.* **1997**, *68*, 3099–3103.

48. Kharintsev, S. S.; Noskov, A. I.; Hoffmann, G. G.; Loos, J. Near-Field Optical Taper Antennas Fabricated with a Highly Replicable AC Electrochemical Etching Method. *Nanotechnology* **2011**, *22*, 025202–025213.

49. Bosman, M.; Ye, E.; Tan, S. F.; Nijhuis, C. A.; Yang, J. K.; Marty, R.; Mlayah, A.; Arbouet, A.; Girard, C.; Han, M.-Y. Surface Plasmon Damping Quantified with an Electron Nanoprobe. *Sci. Rep.* **2013**, *3*, 1312.

50. Nicoletti, O.; de La Peña, F.; Leary, R. K.; Holland, D. J.; Ducati, C.; Midgley, P. A. Three-Dimensional Imaging of Localized Surface Plasmon Resonances of Metal Nanoparticles. *Nature* **2013**, *502*, 80–84.

51. Lazar, S.; Botton, G.; Zandbergen, H. Enhancement of Resolution in Core-Loss and Low-Loss Spectroscopy in a Monochromated Microscope. *Ultramicroscopy* **2006**, *106*, 1091–1103.

52. Bellido, E.; Rossouw, D.; Botton, G. Toward 10 meV Electron Energy-Loss Spectroscopy Resolution for Plasmonics. *Microsc. Microanal.* **2014**, *20*, 767–778.

53. Geuquet, N.; Henrard, L. Eels and Optical Response of a Noble Metal Nanoparticle in the Frame of a Discrete Dipole Approximation. *Ultramicroscopy* **2010**, *110*, 1075–1080.

54. Johnson, P. B.; Christy, R.-W. Optical Constants of the Noble Metals. *Phys. Rev. B: Condens. Matter Mater. Phys.* **1972**, *6*, 4370–4379.

55. Mazzucco, S.; Geuquet, N.; Ye, J.; Stephan, O.; Van Roy, W.; Van Dorpe, P.; Henrard, L.; Kociak, M. Ultralocal Modification of Surface Plasmons Properties in Silver Nanocubes. *Nano Lett.* **2012**, *12*, 1288–1294.

56. The translation between the values of the first LSPR mode's wavelength and energy is made through the relation $\lambda_{LSPR}^{(1)} = hc/E_{LSPR}^{(1)}$, with $h \approx 4.14 \times 10^{-15}$ eV· s being the Planck's constant, and $c \approx 3 \times 10^{17}$ nm/s the speed of light in a vacuum.

57. The signal enhancement is defined as $M = [(I_{tip} - I_{FF})/I_{FF}] \times (A_{FF}/A_{NF})$, where I_{tip} and I_{FF} are the intensities recorded with the tip (near-field signal plus far-field background signal) and without the tip (far-field signal), respectively, and A_{NF} and A_{FF} are the sample areas probed in the near-field (area under the tip) and far-field (focus area) regimes, respectively.[45] In the present experiment, the tip and the focus radii are $r_{tip} \approx 20$ nm and $r_{focus} \approx 275$ nm, respectively, the latter defined by the Rayleigh criterion ($r_{focus} = 0.61\lambda_L/NA$, with $\lambda_L = 632.8$ nm, and NA = 1.4).[45]